Supporting Information
Two-dimensional Ca_4N_2 as a one-dimensional electride $[Ca_4N_2]^{2+}\cdot 2e^-$ with ultrahigh conductance

Xiaofeng Liu,[1] Zijing Ding,[1] Jie Liu,[1] Wei Hu,[1,*] and Jinlong Yang[1,†]

[1] *Hefei National Laboratory for Physical Sciences at Microscale, Department of Chemical Physics, and Synergetic Innovation Center of Quantum Information and Quantum Physics, University of Science and Technology of China, Hefei, Anhui 230026, China*

Table of Contents

*E-mail: whuustc@ustc.edu.cn
†E-mail: jlyang@ustc.edu.cn

The calculations of relaxation time, group velocity and mobility of carrier for monolayer Ca_4N_2

In order to get the transport properties of the interstitial electrons in two-dimensional (2D) Ca_4N_2, we use the QUANTUM-ESPRESSO package[1] to perform density functional theory and density-functional perturbation theory[2] combined with wannier interpolation technique[3] implemented by EPW code[4] to investigate the relaxation time and mobility of carrier. The electronic structures are described by the generalized gradient approximation (GGA) based Perdew-Burke-Erzenhorf (PBE)[5] exchange-correlation functional with the ultrasoft pseudopotentials. The cutoff energies for wave functions and charge density are set 80 Ry and 800 Ry, respectively. A vacuum space of 20 Å is inserted between the periodically repeated slabs. Ground-state calculations are carried out on a regular 24×32×1 mesh of k points with a 0.02 Ry Methfessel-Paxton smearing. Electron group velocity is calculated by using the BOLTZWANN package.[6] The coarse q-mesh for monolayer Ca_4N_2 is taken with 6×8×1 to obtain phonon spectrum by conducting density functional perturbation theory (DFPT) with a 10^{-17} Ry convergence threshold (Fig. S3).

The relaxation time $\tau_{n\mathbf{k}}$ of the interstitial electrons in monolayer Ca_4N_2 is expressed by the imaginary part of electron-phonon (e-ph) self-energy ($\Sigma''_{n\mathbf{k}}(w,T)$):

$$\tau_{n\mathbf{k}}(\omega,T) = \frac{\hbar}{2\Sigma''_{n\mathbf{k}}(\omega,T))} \tag{1}$$

$$\begin{aligned}\Sigma''_{n\mathbf{k}}(\omega,T) &= \pi\Sigma_{m\nu\mathbf{q}}\left|g_{nm\nu}(\mathbf{k},\,\mathbf{q})\right|^2 \\ &\times \left[(N^0_{\nu\mathbf{q}}(T)+f^0_{m\mathbf{k}+\mathbf{q}}(T))\delta(\varepsilon_{n\mathbf{k}}-\varepsilon_{n\mathbf{k}+\mathbf{q}}+\hbar\omega_{\nu\mathbf{q}})\right. \\ &- \left.(N^0_{\upsilon\mathbf{q}}(T)+1-f^0_{m\mathbf{k}+\mathbf{q}}(T))\delta(\varepsilon_{n\mathbf{k}}-\varepsilon_{n\mathbf{k}+\mathbf{q}}+\hbar\omega_{\nu\mathbf{q}})\right]\end{aligned} \tag{2}$$

where $g_{nm\nu}(\mathbf{k},\,\mathbf{q})$ is the e-ph coupling matrix element corresponding to electron scattering from band n at wave vector $\mathbf{k}$ to band m at $\mathbf{k}+\mathbf{q}$ by interacting with a phonon ν with a wave vector $\mathbf{q}$, $\hbar\omega_{\nu\mathbf{q}}$ and $N^0_{\upsilon\mathbf{q}}$ are the phonon energy and the Bose-Einstein distribution and $f(T)$ is the electron distribution function at specific temperature. In our calculations, the energy ranges within 25 meV from the Fermi energy due to the thermal fluctuation at room temperature (300 K). The carrier mobility is calculated by Boltzmann transport equation:

$$\mu = e\frac{\Sigma_n\int\tau(n,\mathbf{k})\upsilon^2(n,\mathbf{k})\frac{\partial f^0_{n\mathbf{k}}}{\partial\varepsilon_{n\mathbf{k}}}d\mathbf{k}}{\Sigma_n\int f^0_{n\mathbf{k}}d\mathbf{k}} \tag{3}$$

where $\upsilon(n,\mathbf{k})$ is the norm of the group velocity, which is expressed by $\upsilon(n,\mathbf{k}) = |1/\hbar\nabla_{\mathbf{k}}\varepsilon_{n\mathbf{k}}|$.

The e-ph coupling is obtained with a relatively coarse $\mathbf{k}$ (12×16×1) and $\mathbf{q}$ (6×8×1) points grids. Then a Wannier-Fourier interpolation[3] method implemented in the EPW code is used to transform e-ph coupling to the Wannier representation with fine grids to calculate the scattering time and mobility. We have test the convergence of the electron linewidth with different $\mathbf{q}$ points (Fig. S4) and obtain a well-converged linewidth with 360×480×1 $\mathbf{q}$ grids. After that, the calculated converged mobility with a fine $\mathbf{k}$ grid (360×480×1) is 215 $cm^2{\cdot}V^{-1}{\cdot}s^{-1}$. The convergence of mobility with different $\mathbf{k}$ grids from 60×80×1 to 480×640×1 with an interval of 60×80×1 is shown in Fig. S5. The relaxation time is also obtained with a fine $\mathbf{k}$ and $\mathbf{q}$ grids (360×480×1). The relaxation time for anionic electrons in Ca_4N_2 ranges from 1.26 to 15.37 fs at the Fermi level, which is comparable to that in Ca_2N (3.82 to 11.63 fs).[7] The group velocity of Ca_4N_2 varies from 0.04 $\sim$ 0.46 × 10^6 $m{\cdot}s^{-1}$ at the Fermi level and 0.01 $\sim$ 0.46 × 10^6 $m{\cdot}s^{-1}$ in the ±25 meV (Fig. S5), when the group velocity of Ca_2N monolayer ranges from 0.13 to 0.36× 10^6 $m{\cdot}s^{-1}$.[7] These two aspects result in the calculated intrinsic mobility of monolayer Ca_4N_2 comparable to that of monolayer Ca_2N (189 $cm^2{\cdot}V^{-1}{\cdot}s^{-1}$). At low temperature 10 K, the relaxation time for anionic electrons in Ca_4N_2 ranges from 0.25 to 2.33 ps at the Fermi level, when it ranges from 0.68 to 5.86 ps at the Fermi level at 2 K.

Multi-layer and bulk Ca_4N_2

The electronic properties of multi-layer structures stacked by monolayer Ca_4N_2 are also investigated. For the two-layer Ca_4N_2, we have explored probable stacked models. After optimization, the most stable model is shown in Fig. S18a. In addition, the stacked models of three, and four-layer Ca_4N_2 are also same as that of two-layer Ca_4N_2. The electronic band structures of multi-layer Ca_4N_2 are given in Fig. S17. They are 2n (n = 2, 3, and 4) bands crossing the Fermi energy level corresponding to the anionic electron bands for two, three, and four-layer Ca_4N_2, respectively. The PED integrated in the energy region within 0.1 eV below the Fermi level and planar averaged charge density for multi-layer Ca_4N_2 are also given in Fig. S18. Their PED maps clearly show that electrons are mainly localized in the channels of multi-layer Ca_4N_2 to form 1D electron states. The planar averaged charge density along the z direction also quantifies the localization features. The ELFs of multi-layer Ca_4N_2 are presented in Fig. S19. There are non-unclear maxima in the channels of the multi-layer Ca_4N_2 plane and interspace between Ca_4N_2 layers, indicating these multi-layer Ca_4N_2 are also electrides.

The above calculations manifest the Ca_4N_2 monolayer and its corresponding multi-layer structure are electrides. The properties of bulk phase are also investigated. The most stable stacked model for bulk phase is same as that of multi-layer structures (Fig. S18). Dynamic stability and thermal stability are carefully checked for the bulk structure. Bulk Ca_4N_2 doesn't show any negative phonon frequencies in the whole Brillouin zone (Fig. S20). We monitor the time evolution of potential energy during the AIMD simulations as presented in Fig. S20b. The potential energy value reaches equilibrium very quickly and fluctuates near the equilibrium value.

The electronic structures of the bulk phase of Ca_4N_2 are given in Fig. S14-16. Its ELF is also examined carefully. In the empty space between cationic layers, ELF attractors are clearly seen in Fig. S19d, which indicates bulk Ca_4N_2 is an electride. The energy bands along ΓXMYΓ and ZURTZ are disperse while they are less disperse along ΓZ, which indicates the electrons distribution on the empty space between Ca_4N_2 layers. The PED map in the energy region within 0.1 eV below the Fermi level is shown in Fig. S18d, where a substantial portion of electron charges are localized in the channels between cationic layers. The localization feature is further quantified by planar averaged charge density along the z direction as well (Fig. S18). We also evaluate the amount of anionic electrons near the Fermi level E_f (i.e., the portion of electrons confined in the 2D empty space among the total electron). It is defined as

$$\begin{aligned} P_{ani} &= \frac{\int_{V_{emp}} dr \int_{E_f-\Delta E}^{E_f+\Delta E} n(r,E)dE}{\int_V dr \int_{E_f-\Delta E}^{E_f+\Delta E} n(r,E)dE)} \\ &= \frac{\iint_A dxdy \int_{z'} dz \int_{E_f-\Delta E}^{E_f+\Delta E} n(r,E)dE}{\int_V dr \int_{E_f-\Delta E}^{E_f+\Delta E} n(r,E)dE} \end{aligned} \tag{4}$$

where V_{emp} is volume of empty space and z' coordinate is only in interlayer space.[8] Depending on the definition, the calculation portion of electrons for bulk Ca_4N_2 is 0.9, which indicates a significant amount of electrons near the Fermi level are located in the interlayer space. Because of the interlayer electron distribution, Ca_4N_2 is expected to have low work function. We have calculated the work function on the surface (001), the (001) surface is cleaved parallel through interlayer space. The work function of surface (001) is 2.97 eV, which is comparable to that of other 2D electrides with the values of $2.58 \sim 2.8$ eV.[9]

S1. Mechanical properties, Young's modulus E(θ) and Poisson's ratio ν (θ)

$$E(\theta) = \frac{Y_{zz}}{\cos^4\theta + d_2\cos^2\theta\sin^2\theta + d_3\sin^4\theta} \tag{5}$$

$$\nu(\theta) = \frac{\nu_{zz}\cos^4\theta - d_1\cos^2\theta sin^2\theta + \nu_{zz}sin^4\theta}{\cos^4\theta + d_2\cos^2\theta\sin^2\theta + d_3\sin^4\theta} \tag{6}$$

$$\nu_{zz} = \frac{C_{12}}{C_{22}} \tag{7}$$

$$d_1 = \frac{C_{11}}{C_{22}} + 1 - \frac{C_{11}C_{22} - C_{12}^2}{C_{22}C_{66}} \tag{8}$$

$$d_2 = -\left(2\frac{C_{11}}{C_{22}} - \frac{C_{11}C_{22} - C_{12}^2}{C_{22}C_{66}}\right) \tag{9}$$

$$d_3 = \frac{C_{11}}{C_{22}} \tag{10}$$

$$Y_{zz} = \frac{C_{11}C_{22} - C_{12}^2}{C_{22}} \tag{11}$$

TABLE S1: The information of lattice constants, bond length (Å) and the cohesive energies (eV) of monolayer Ca_4N_2, Sr_4N_2 and Ca_2N. AE represents the alkaline earth metal atoms (Ca, Sr).

Electride	a	b	AE-N1	AE-N2	AE-N3	AE-AE	E_b
Ca_4N_2	4.84	3.52	2.32	2.47	2.46	3.23	0.68
Sr_4N_2	5.25	3.71	2.47	2.63	2.66	3.50	0.53
Ca_2N	3.56	-	2.41	-	-	3.56	0.61

TABLE S2: The adsorption energies (eV) of molecules (H_2O, N_2, O_2, and H_2) on monolayer Ca_4N_2 and G/Ca_4N_2/G

	H_2O	N_2	O_2	H_2
Ca_4N_2	-1.02	-1.16	-11.76	-2.03
G/Ca_4N_2/G	-0.16	-0.09	0.10	-0.07

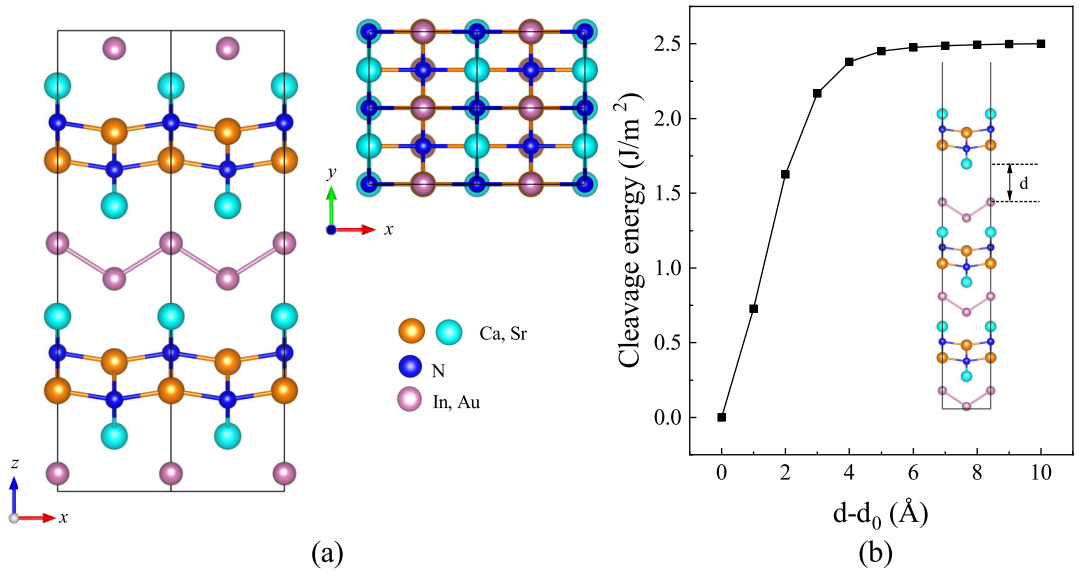

FIG. S1: (a) Top and side views of $Ca_4M_2N_2$. Blue spheres denote the N atom. Cyan and orange spheres denote Ca atoms and purple spheres denote the In atoms, respectively. (b) The relationship between cleavage energy and the interlayer distance. d_0 denotes the interlayer distance under equilibrium. The insert describes the cleavage process of monolyer Ca_4N_2.

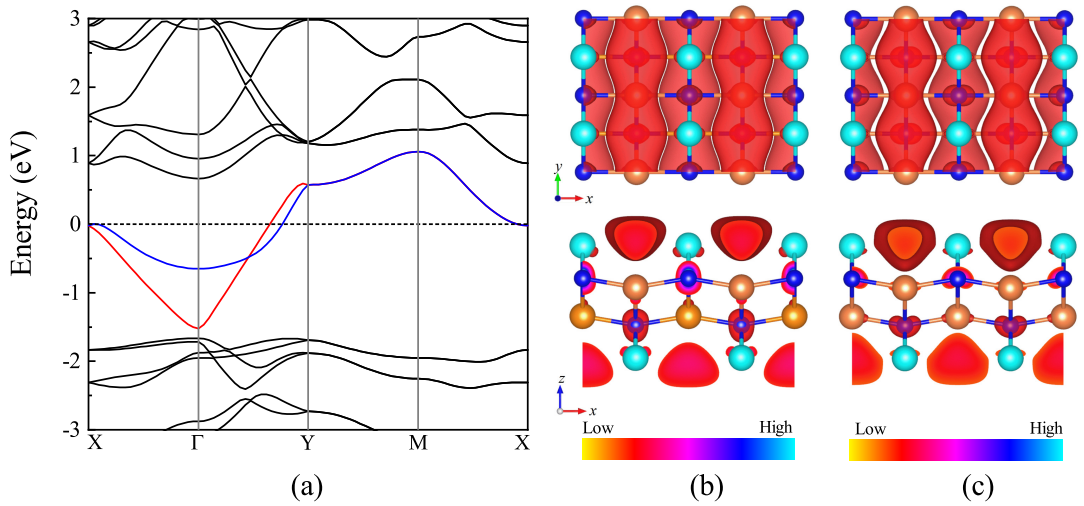

FIG. 2: (a) The band structure with high-symmetric k-point paths along X(0.5, 0, 0)-Γ(0, 0, 0)-Y(0, 0.5, 0)-M(0.5, 0.5, 0)-X(0.5, 0, 0) with PBE functional for monolayer Ca_4N_2. (b, c) Top and side views of the partial electron density integrated in the energy region within 0.1 eV below the Fermi level with the isosurfaces value of 1.35×10^{-3} e·Å^{-3} corresponding to linear-band and parabola-band, respectively.

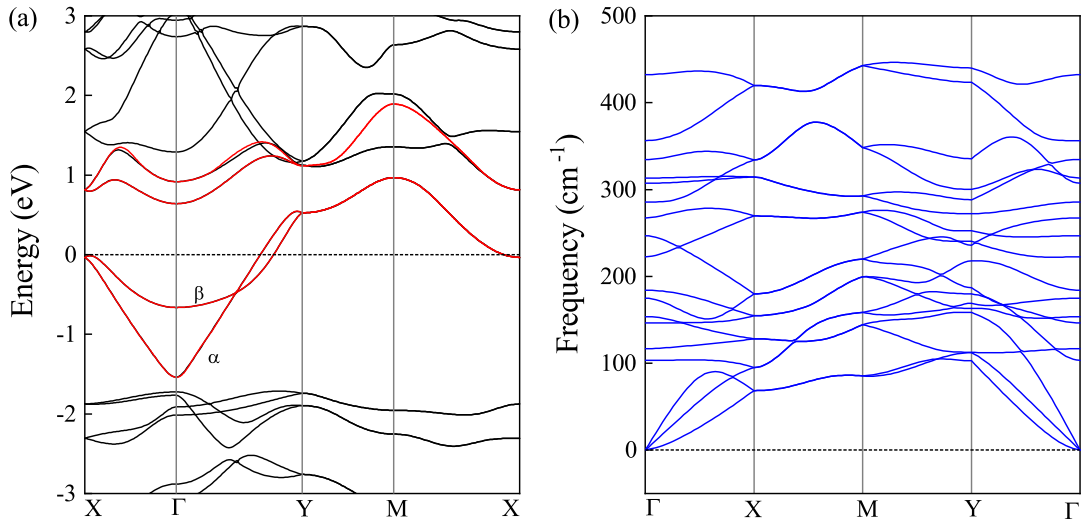

FIG. S3: (a) Electron and (b) phonon band structures for monolayer Ca_4N_2. Results from wannier interpolation are plotted with red dots. The Fermi level is set to zero.

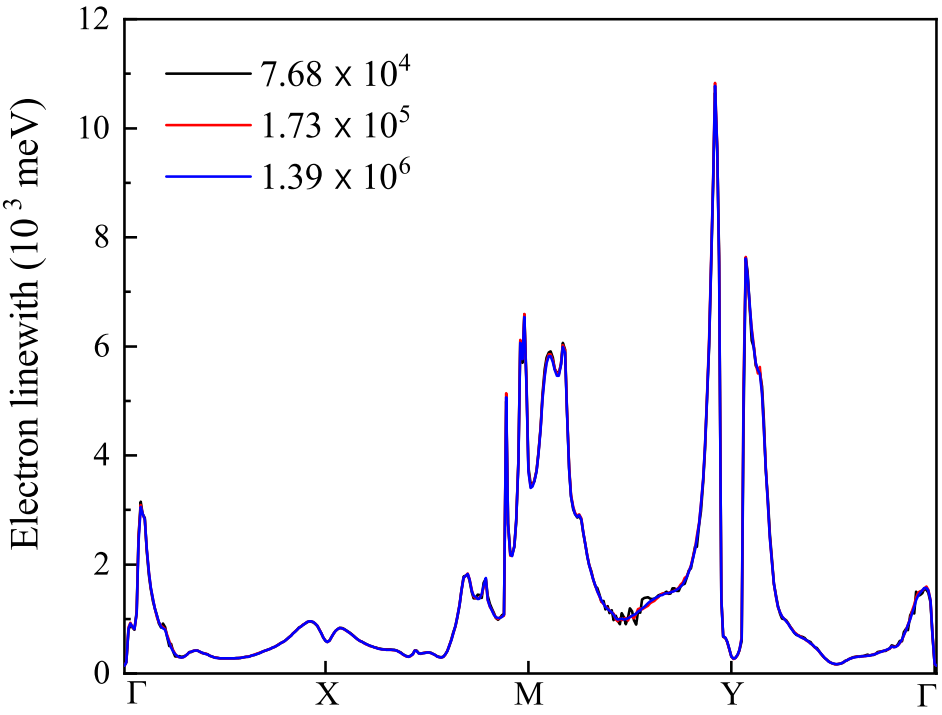

FIG. S4: Electron linewidth for the linear-band calculated along high-symmetry **k** points. Black, red, and blue lines represent electron linewidth calculated with the numbers of **q** grids with 240×320×1, 360×180×1, and 1020×1360×1, respectively.

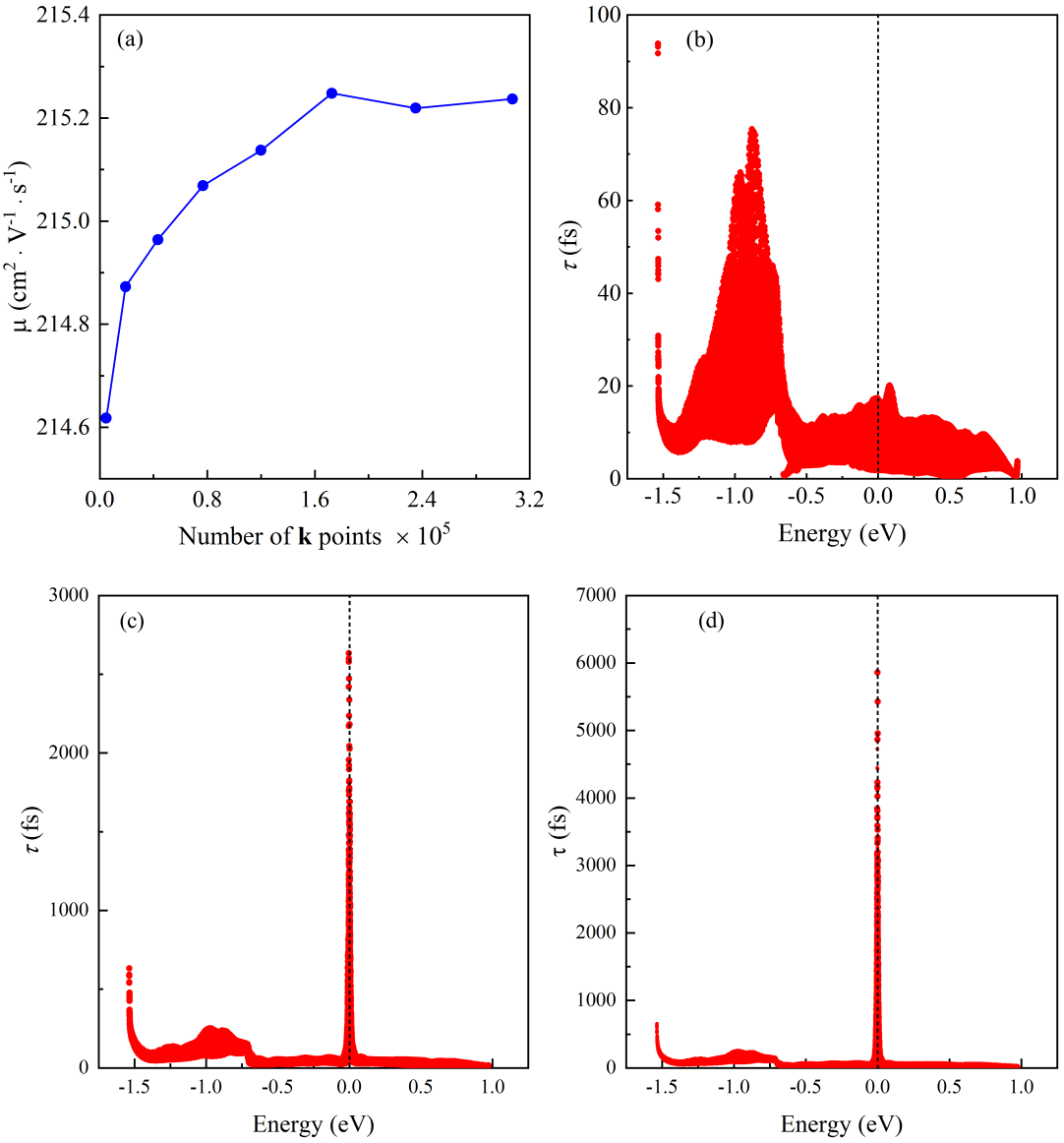

FIG. S5: (a) The convergence of calculated carrier mobility by using a 360×420×1 **q** grid with different numbers of **k** points. (b) Relaxation time for α and β bands (shown in Fig. S3) at 300K in monolayer Ca_4N_2. (c, d) Relaxation time for α and β bands at 10 K and 2 K. The Fermi level is set to zero.

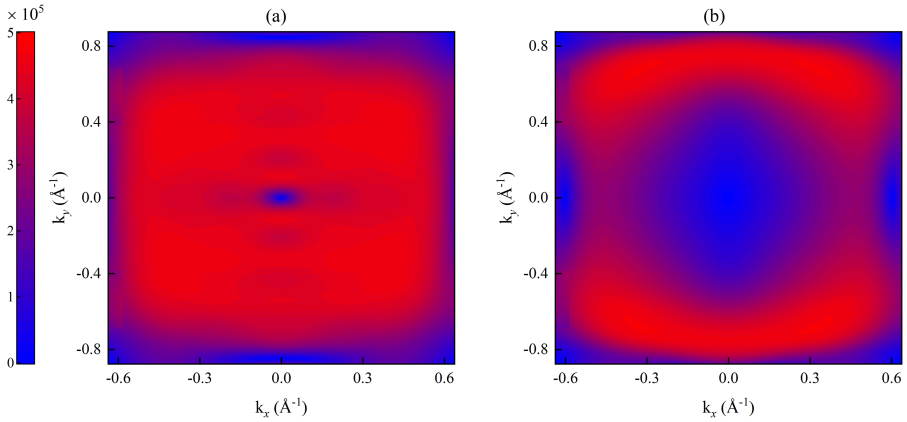

FIG. S6: Electron group velocity $v(\mathrm{n},\mathbf{k})$ ($\mathrm{m{\cdot}s^{-1}}$) for (a) α and (b) β bands of monolayer Ca_4N_2

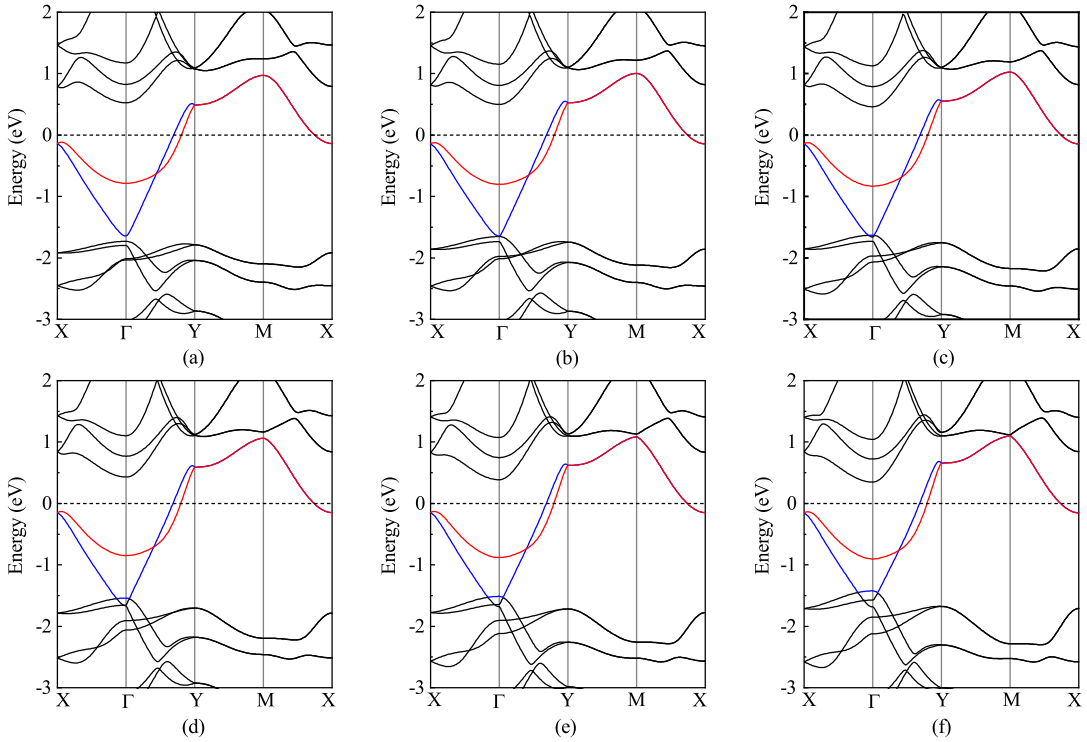

FIG. S7: The band structures of monolayer Ca_4N_2 under compression, (a) 1%, (b) 2%, (c) 3%, (d) 4%, (e) 5%, and (f) 6%. The Fermi levels are set to zero. The red and blue bands denote the interstitial bands of the anionic electrons.

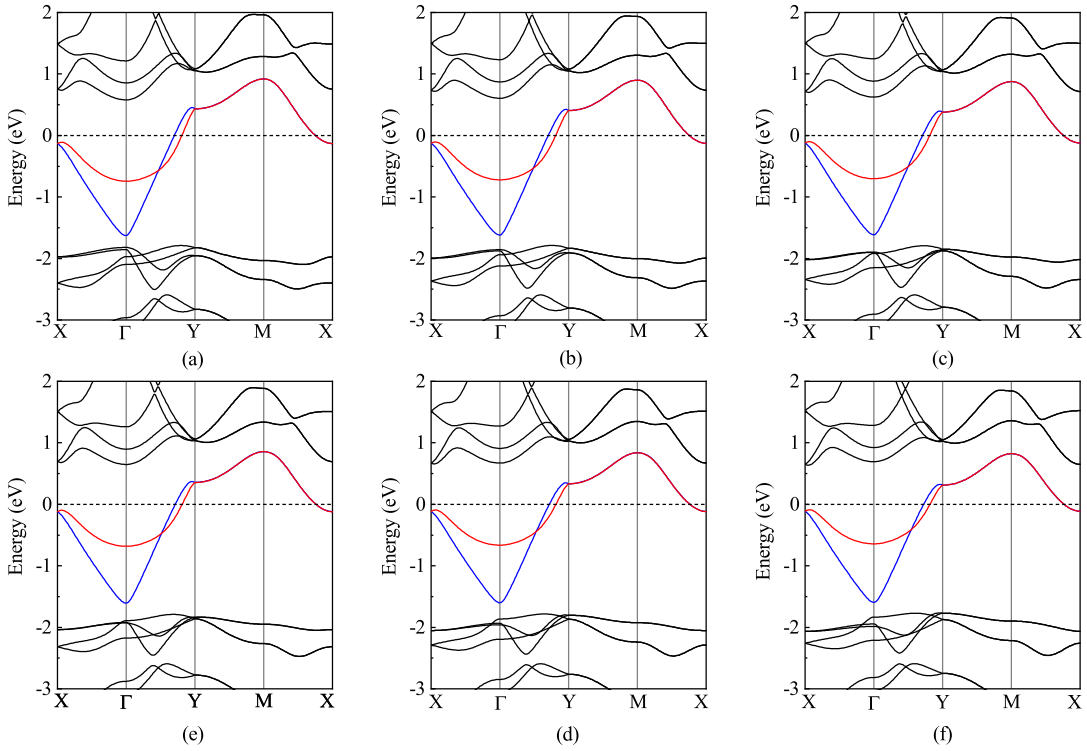

FIG. S8: The band structures of monolayer Ca_4N_2 under tensile strains, (a) 1%, (b) 2%, (c) 3%, (d) 4%, (e) 5%, and (f) 6%. The Fermi levels are set to zero. The red and blue bands denote the interstitial bands of the anionic electrons.

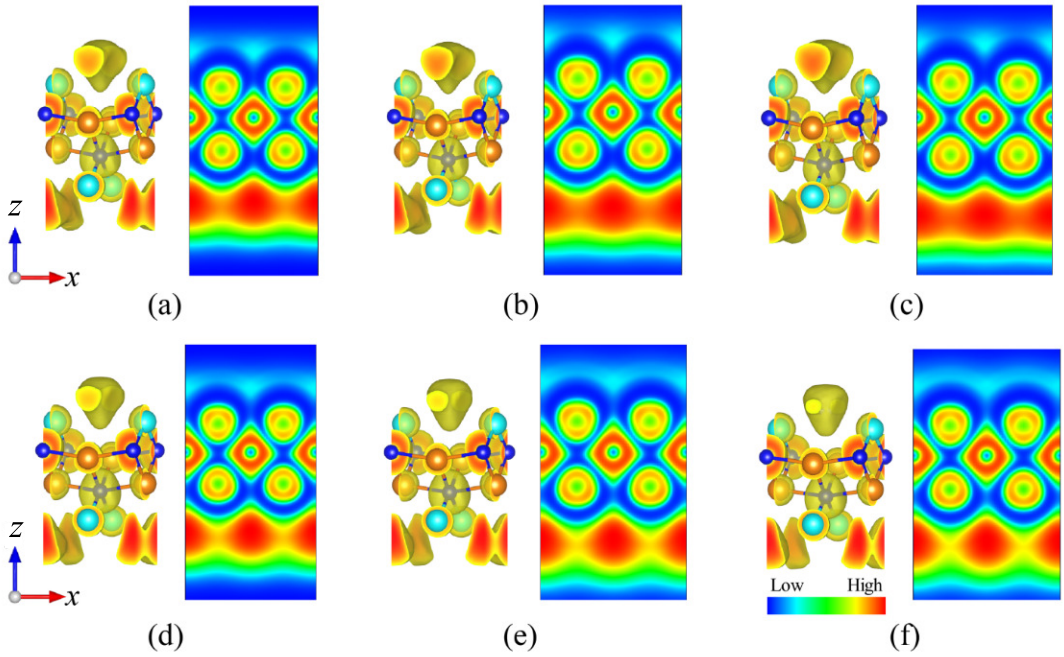

FIG. S9: The electron localization functions (left) with the isosurfaces value of 0.65 and the (100) plane under (a-c) compression (2%, 4%, and 6%) and (d-f) tensile strains (2%, 4%, and 6%) for monolayer Ca_4N_2.

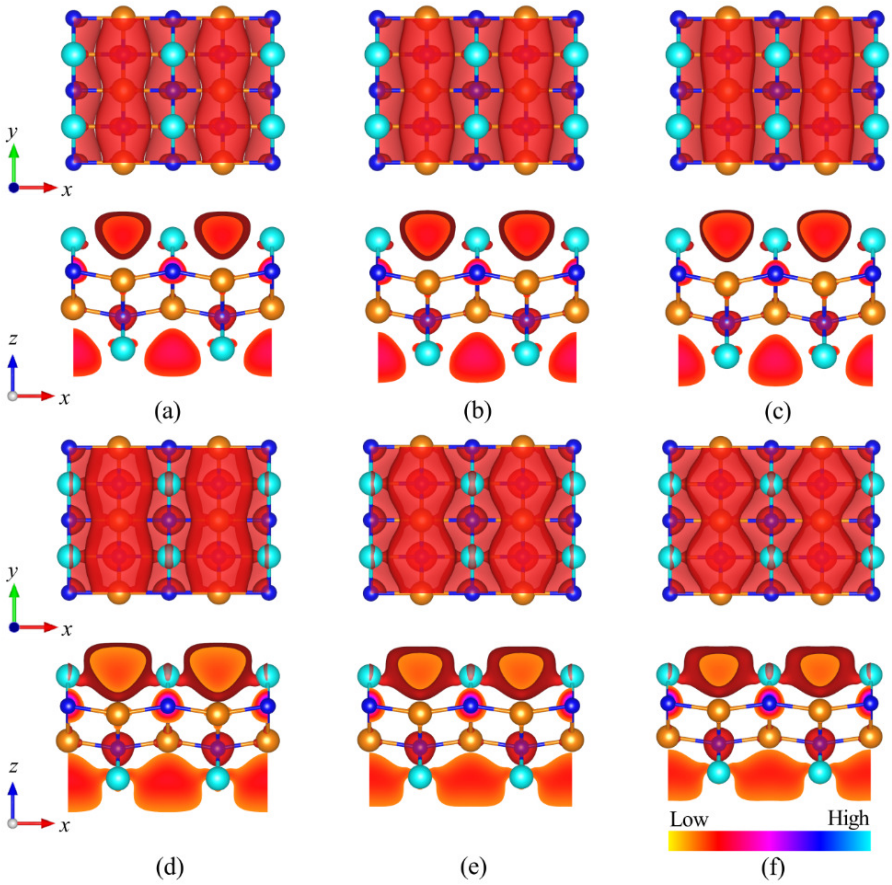

FIG. S10: Top and side views of the partial charge density integrated in the energy region within 0.1 eV below the Fermi level with the isosurfaces value of 2.70×10^{-3} e·Å^{-3} under (a-c) compression (2%, 4%, and 6%) and (d-f) tensile strains (2%, 4%, and 6%) for monolayer Ca_4N_2.

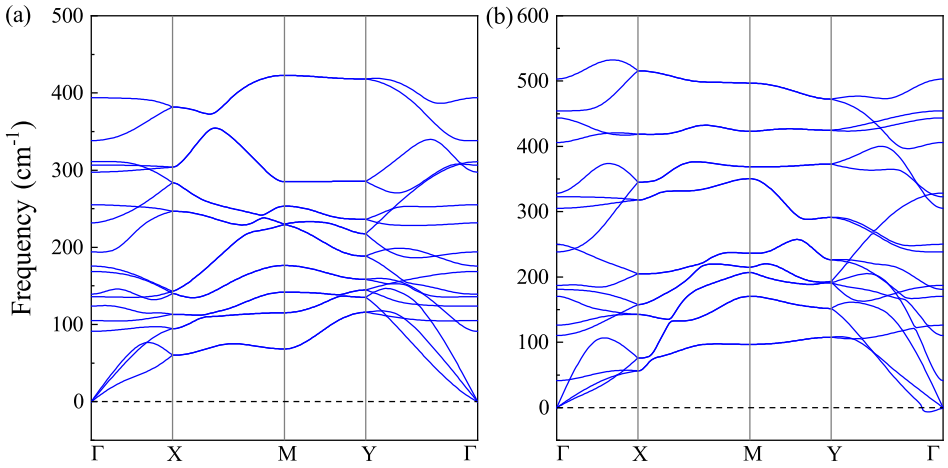

FIG. S11: (a, b)The phonon pectrum of monolayer Ca_4N2*under*± 6 % biaxial strain.

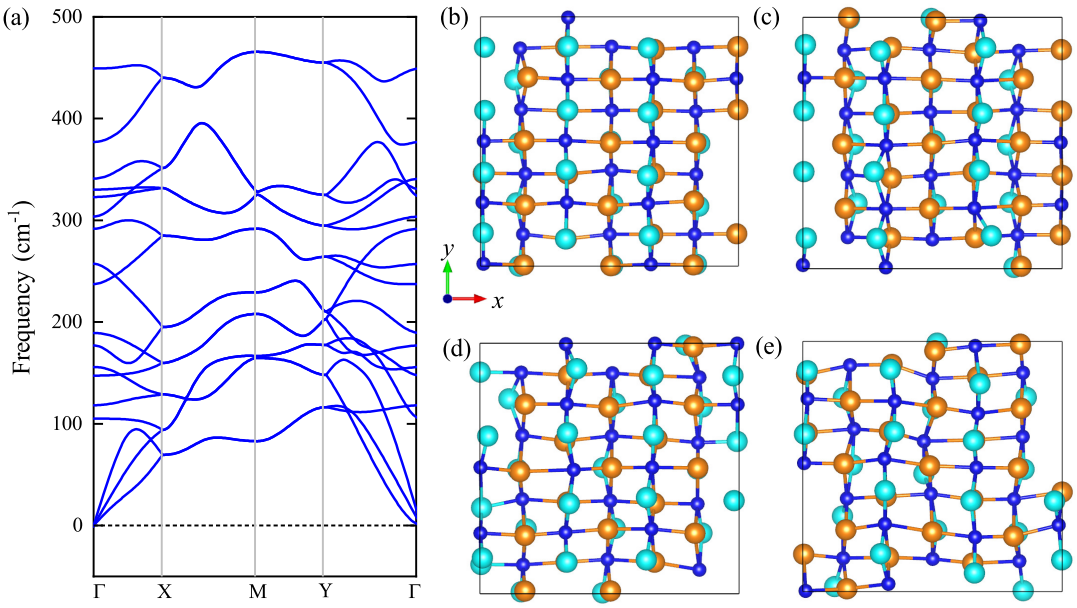

FIG. S12: (a) The phonon spectrum and the structure snapshots at T = (b) 300, (c) 600, (d) 900, and (e) 1200 K of the Ca_4N_2 monolayer at the end of 4 ps AIMD simulations.

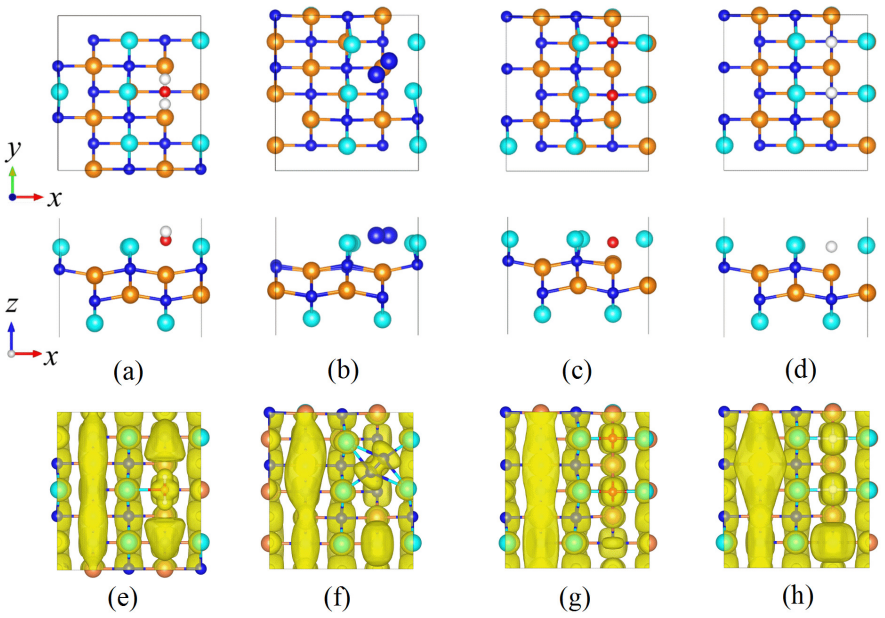

FIG. S13: The configurations and electron localiztion function of 2D Ca_4N_2 with a 2×3×1 supercell after moleculs adsorption, (a e) H_2O, (b, f) N_2, (c, g) O_2, and (d, h) H_2 adsorption on 2D Ca_4N_2. Orange and cyan balls represent the Ca atoms. Blue, red, and white balls denote nitrogen, oxygen, and hydrogen atoms, respectively.

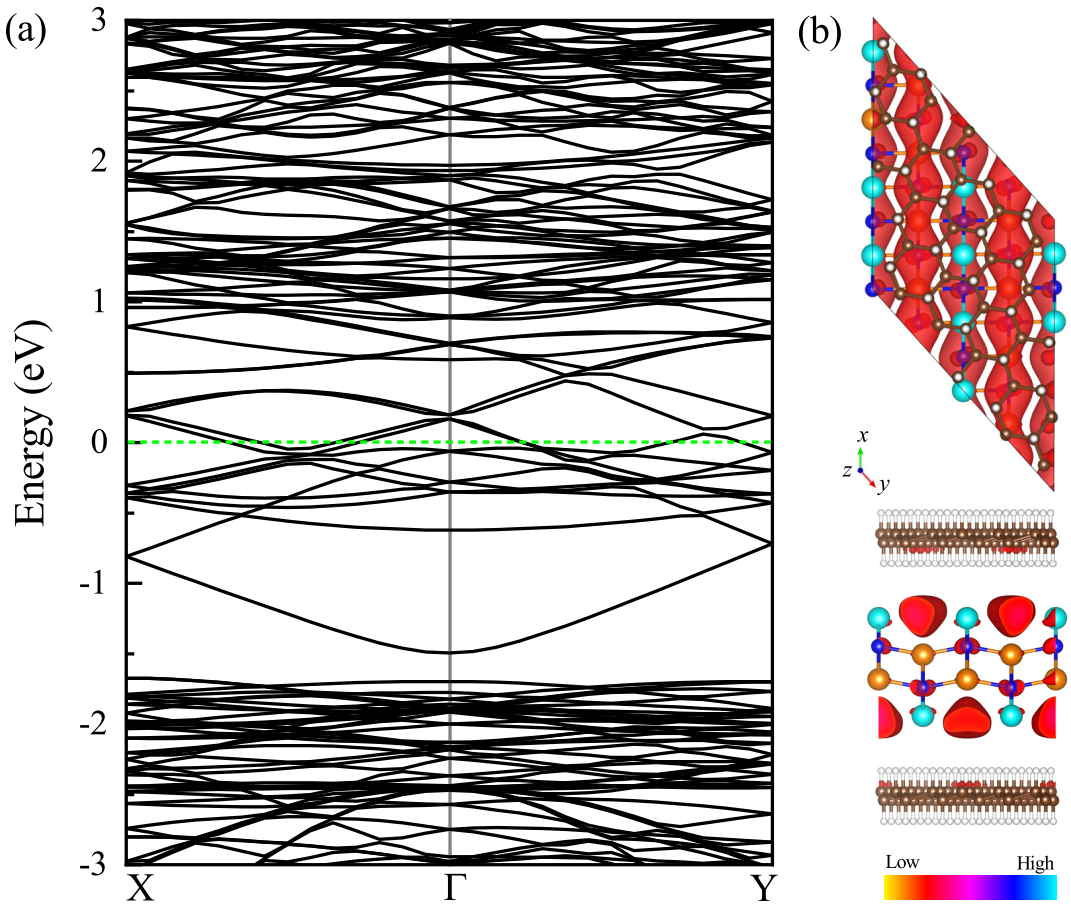

FIG. S14: (a) Band structure of $G/Ca_4N_2/G$ heterostructure. (b) Top and side views of the partial charge density integrated in the energy region within 0.1 eV below the Fermi level with the isosurfaces value of 4.70×10^{-3} e·Å^{-3} Orange and cyan balls represent the Ca atoms. Blue, grey, and white balls denote nitrogen, carbon, and hydrogen atoms, respectively.

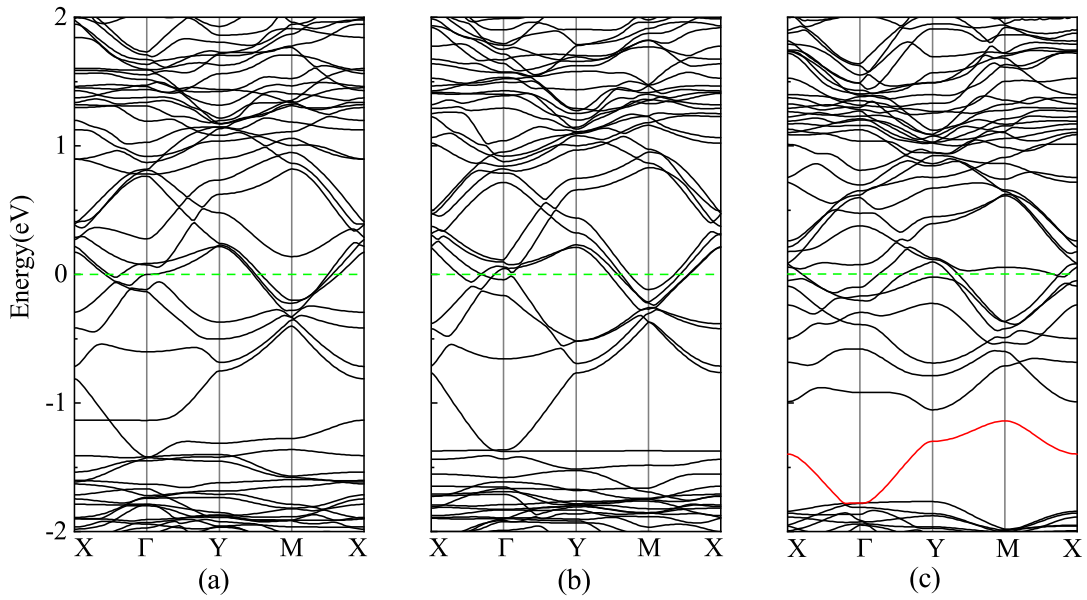

FIG. S15: The band structures of the 2×3×1 supercell Ca_4N_2 monolayer with point defects, (a) V_{Ca2}, (b) V_{Ca4}, and (c) V_N.

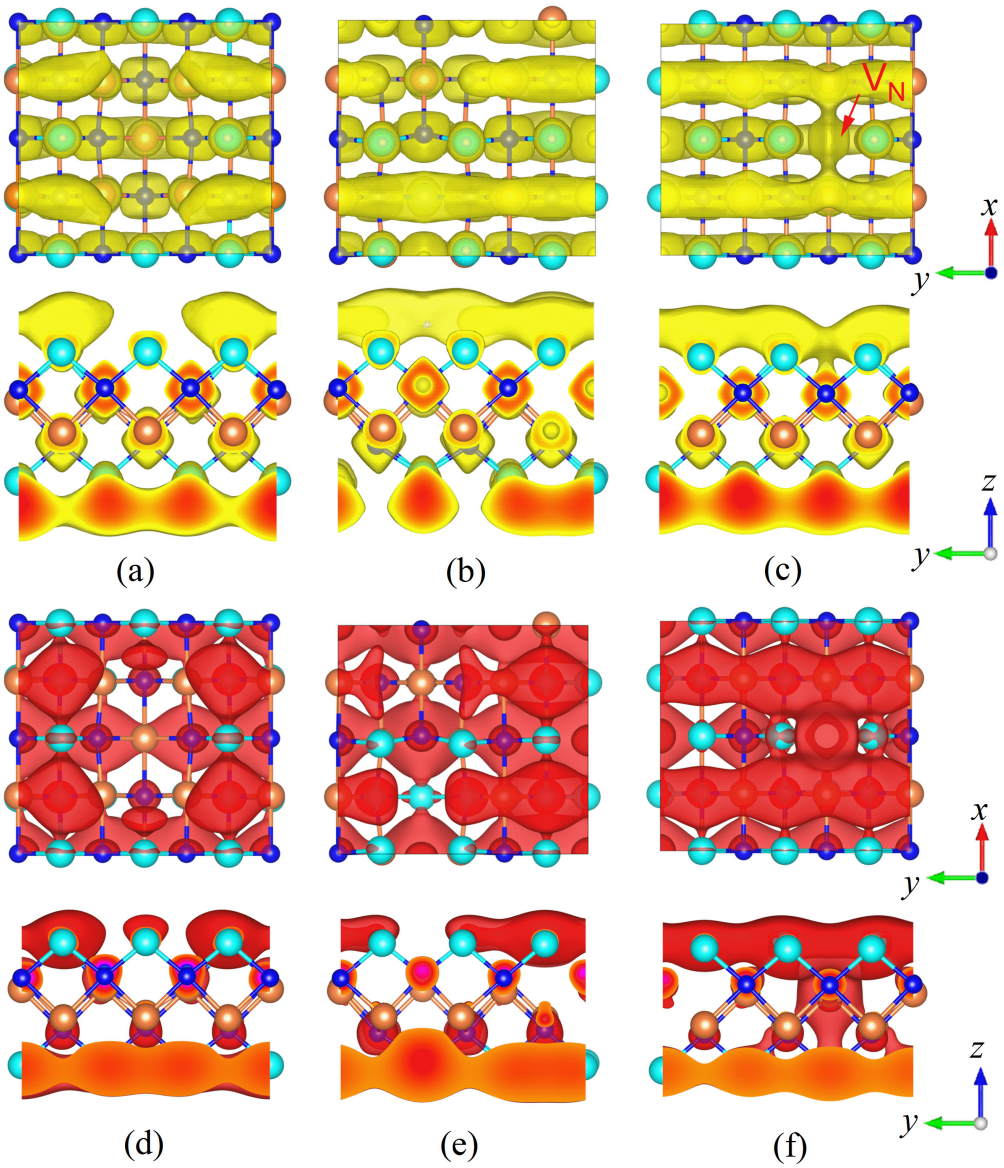

FIG. S16: The electron localization function of (a) V_{Ca2}, (b) V_{Ca4} and (c) V_N with the value of 0.65. The partial charge density of integrated in the energy region within 0.2 eV below the Fermi level with the isosurfaces value of 3.38×10^{-3}, 5.4×10^{-3}, and 5.4×10^{-3} e·Å^{-3} for (d) V_{Ca2}, (e) V_{Ca4}, and (f) V_N, respectively.

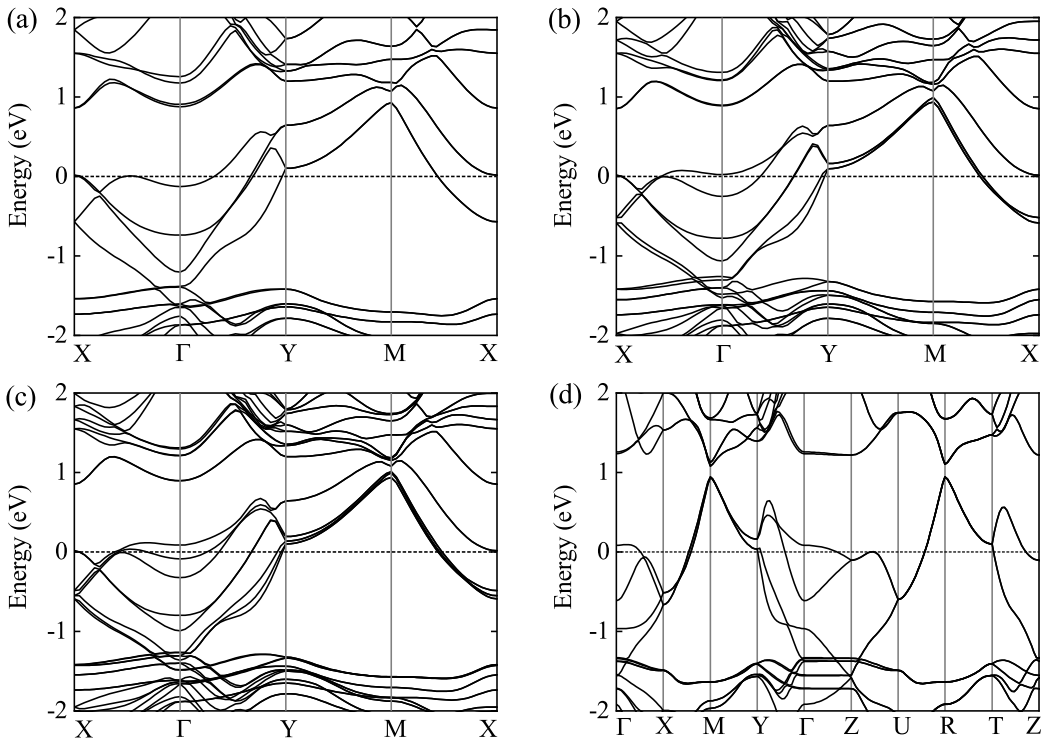

FIG. S17: The band structures of (a) two, (b) three, (c) four-layer, and (d) bulk Ca_4N_2. The Fermi levels are set to zero.

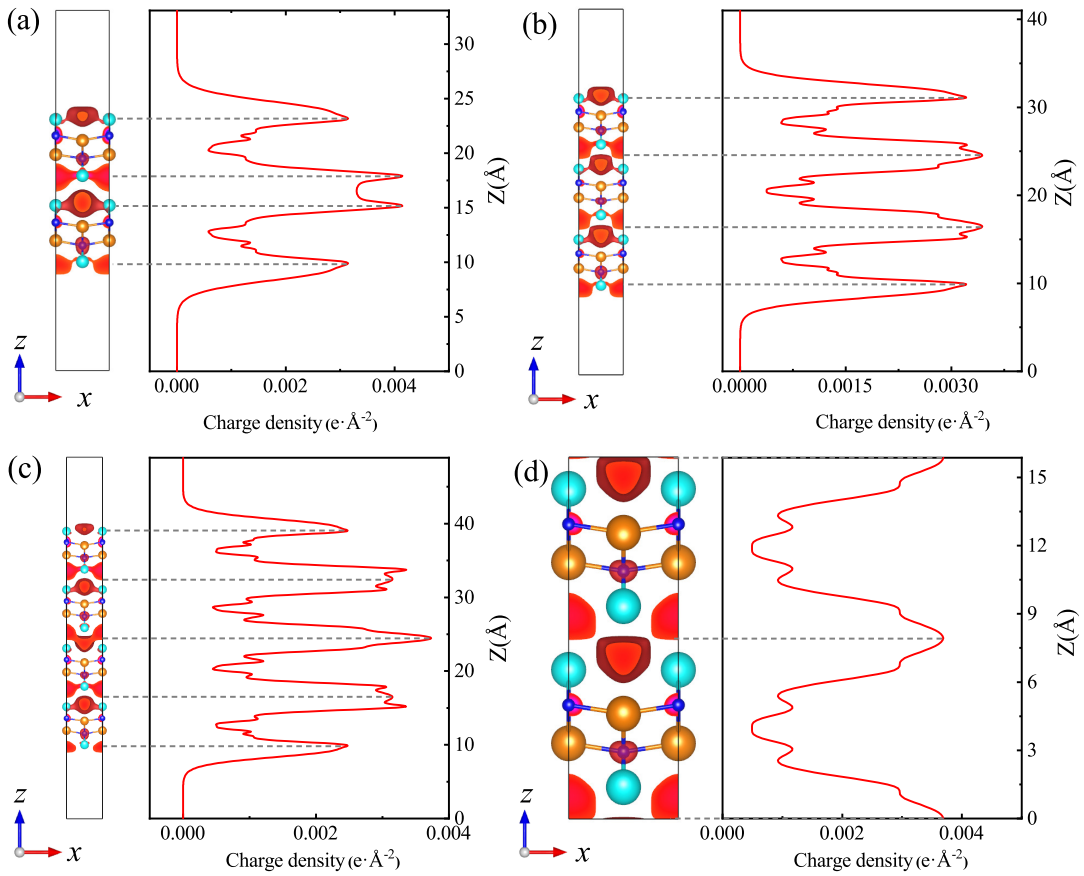

FIG. S18: The partial electron density integrated in the energy region within 0.1 eV below Fermi energy with the isosurfaces value of 3.37×10^{-3} e·Å^{-3} (left) and planar averaged charge density along the z direction (right) for (a)two, (b) three, (c) four-layer, and (d) bulk Ca_4N_2.

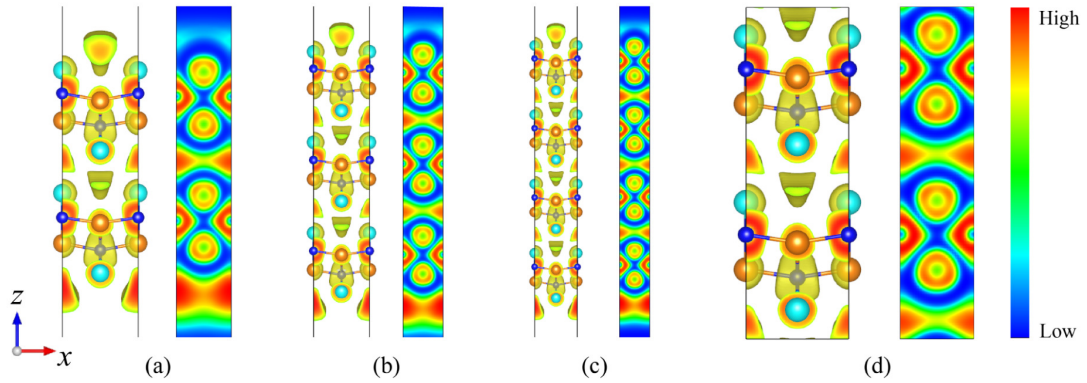

FIG. S19: The electron localization function with the isosurfaces value of 0.55 (left) and the (100) plane (right) for (a) two, (b) three, (c) four-layer and (d) bulk Ca_4N_2.

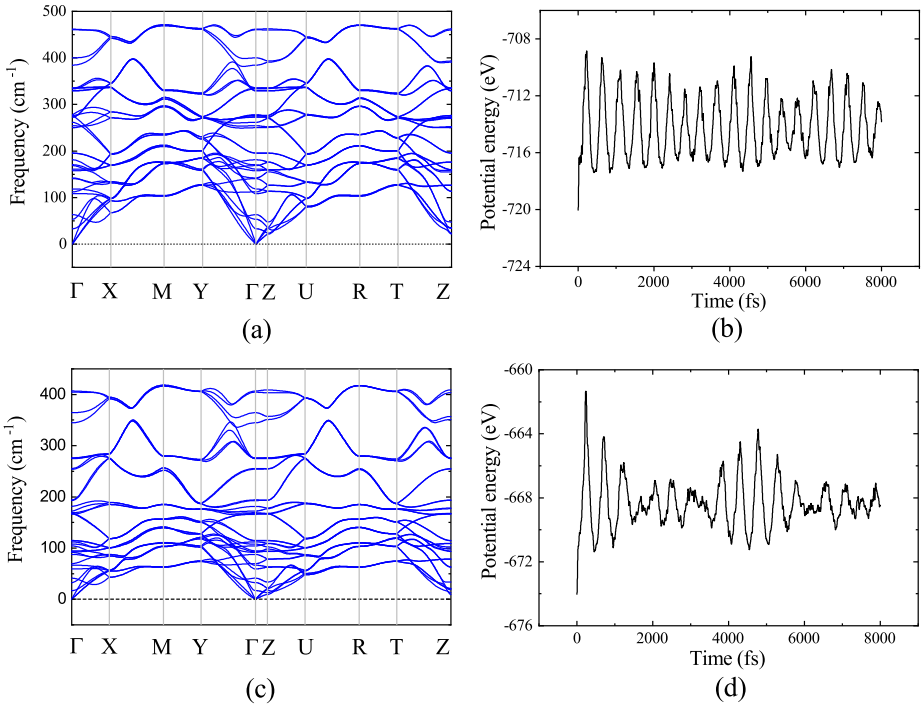

FIG. S20: The phonon spectrums and the evolution of potential energy over time for bulk Ca_4N_2 (a, b) and Sr_4N_2 (c, d).

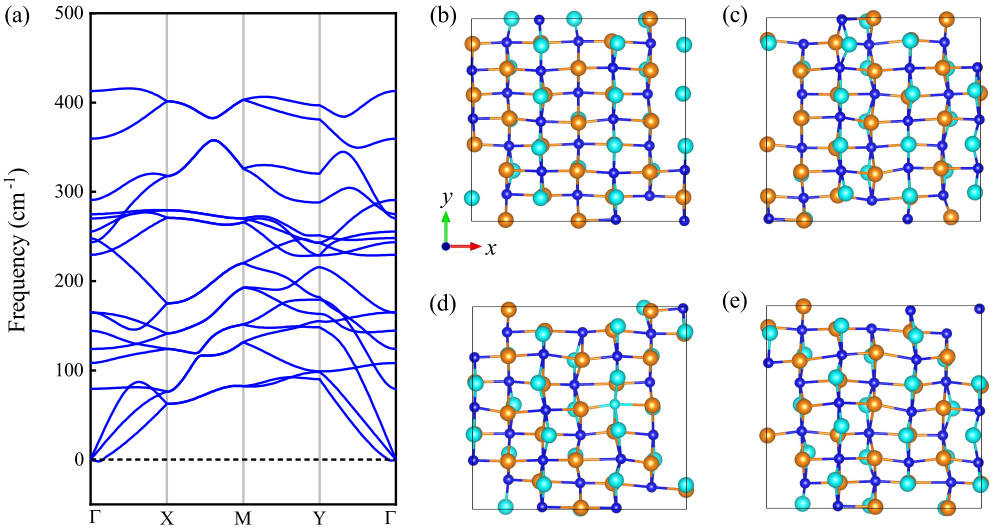

FIG. S21: (a) The phonon spectrum and the structure snapshots at T = (b) 300, (c) 600, (d) 900, and (e) 1200 K of the Sr_4N_2 monolayer at the end of 4 ps AIMD simulations.

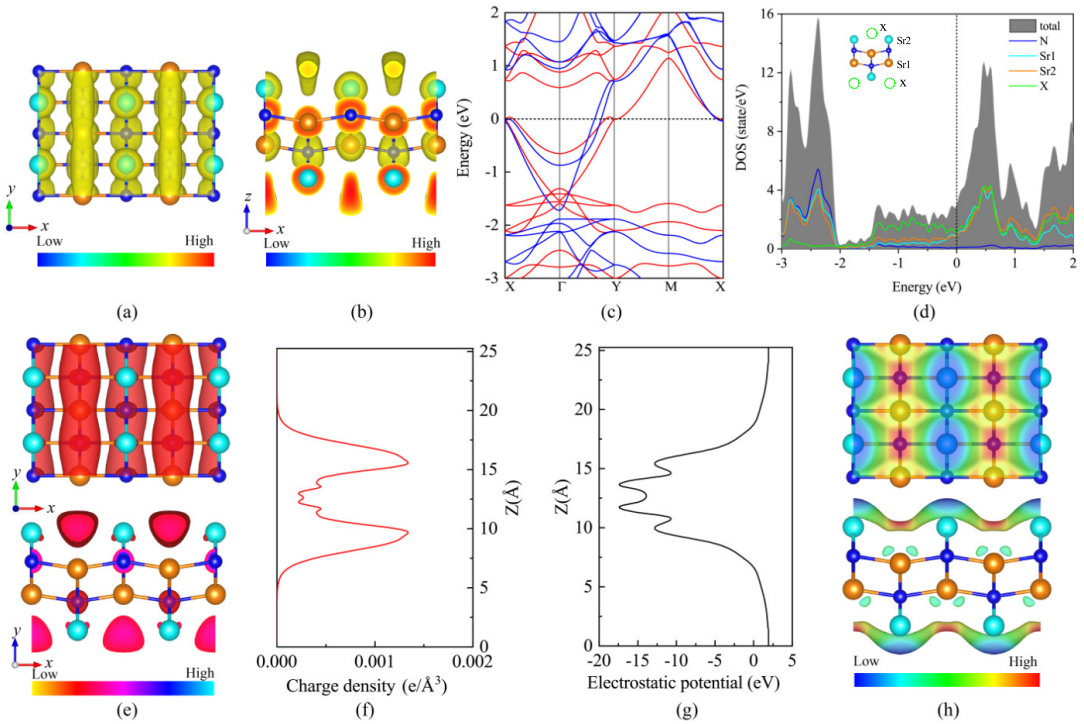

FIG. S22: (a, b) The top and sides view of electron localization function with the isosurfaces value of 0.65. (c) The band structure with high-symmetric k-point paths along X(0.5, 0, 0)-Γ(0, 0, 0)-Y(0, 0.5, 0)-M(0.5, 0.5, 0)-X(0.5, 0, 0) with PBE (red) and HSE06 (blue) functionals. (d) Total density of states and projected density of states for monolayer Sr_4N_2. Sr1, Sr2, and X (green dash balls) denote the Sr atoms of the middle two SrN layers, the Sr atoms of top and bottom layers, and the anionic electrons in the channels for monolayer Sr_4N_2. The density of states of the anionic electrons are projected by adding a pseudo-atom with a Wigner-Seitz radius of 2.20 Å in the position corresponding to localized non-nuclear maximum of the ELF. (e, f) The partial electron density integrated in the energy region within 0.1 eV below the Fermi level with the isosurfaces value of 1.69×10^{-3} e·Å^{-3} and planar averaged charge density along the z direction. (g) The electrostatic potential along z direction for monolayer Sr_4N_2. (h) The top and side views of isosurfaces of electron density colored with electrostatic potential. The equi-density level is 0.034 e·Å^{-3} and the electrostatic potential ranges from -8 eV (blue) to -4 eV (red). The Fermi level is set to zero.

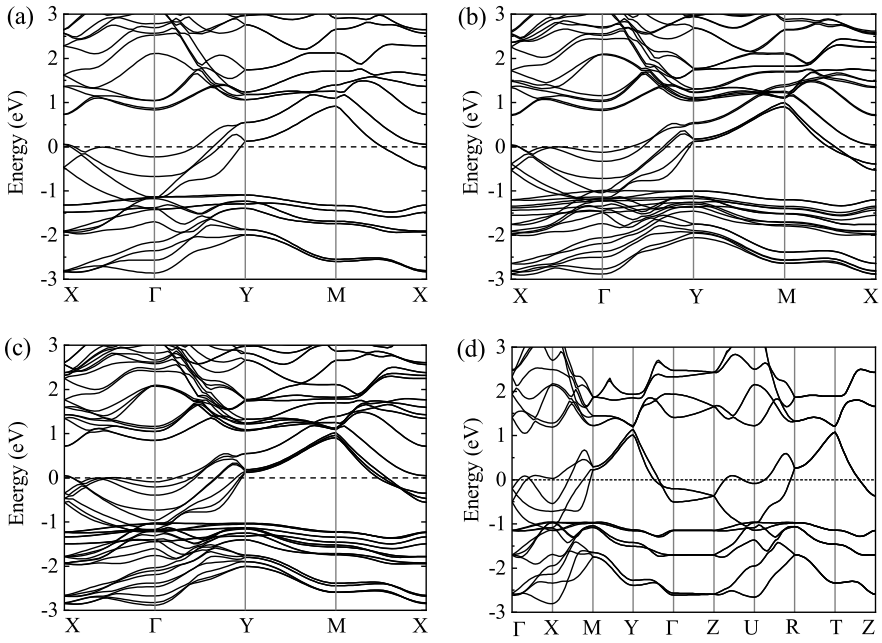

FIG. S23: The band structures of (a) two, (b) three, (c) four-layer, and (d) bulk Sr_4N_2. The dash lines denote the Fermi level.

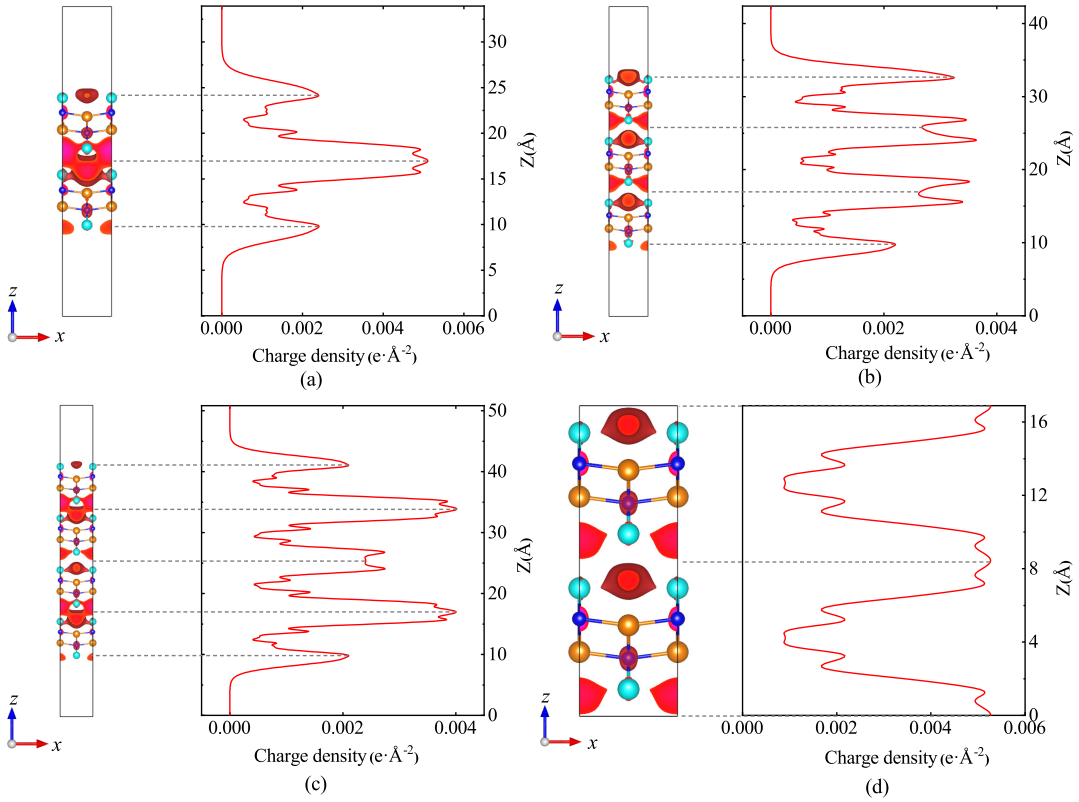

FIG. S24: The partial electron density integrated in the energy region within 0.1 eV below the Fermi energy with the isosurfaces value of 3.38×10^{-3} e·Å^{-3} (left) and planar averaged charge density along the z direction (right) for (a) two, (b) three, (c) four-layer and (d) bulk Sr_4N_2.

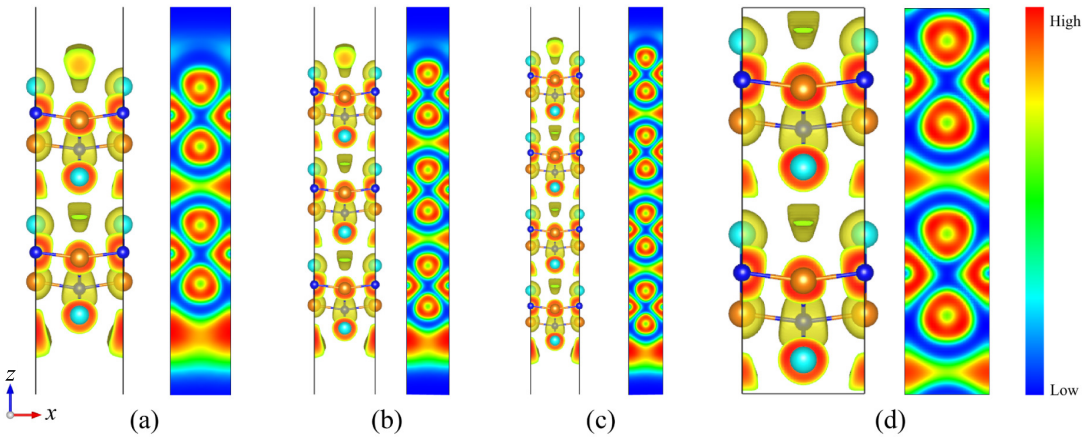

FIG. S25: The electron localization function with the isosurfaces value of 0.55 (left) and the (100) plane (right) for (a) two, (b) three, (c) four-layer and (d) bulk Sr_4N_2.

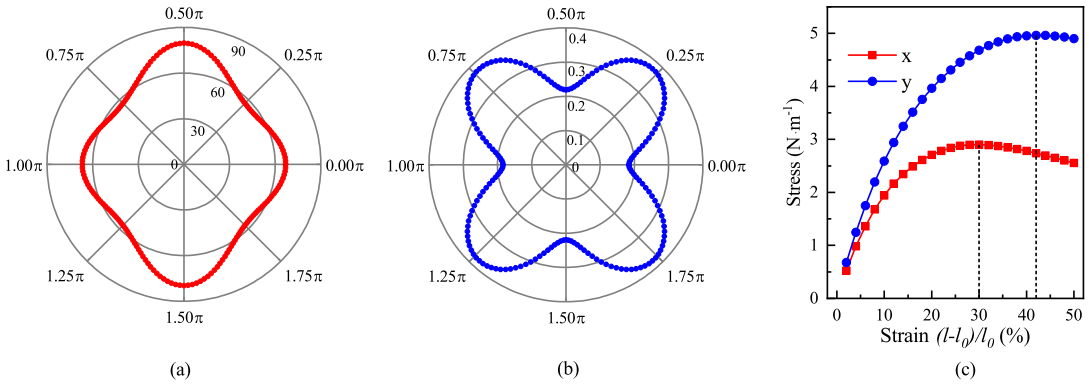

FIG. S26: The mechanical properties of monolayer Sr_4N_2. The orientation-dependent (a) Young's modulus, (b) Poisson's ratio and (c) strain-stress relation. The tensile strain is defined as $(l\text{-}l_0)/l_0$ varying from 0 to 50%, where l_0 and l are the equilibrium lattice constant and the strained one. The vertical dashed black lines indicate the critical strains along x and y directions.

[1] P. Giannozzi, S. Baroni, N. Bonini, M. Calandra, R. Car, C. Cavazzoni, D. Ceresoli, G. L. Chiarotti, M. Cococcioni, I. Dabo, et al., J. Phys. Condens. Matter **21**, 395502 (2009).
[2] S. Baroni, S. De Gironcoli, A. Dal Corso, and P. Giannozzi, Rev. Mod. Phys. **73**, 515 (2001).
[3] A. A. Mostofi, J. R. Yates, Y.-S. Lee, I. Souza, D. Vanderbilt, and N. Marzari, Comput. Phys. Commun. **178**, 685 (2008).
[4] S. Poncé, E. R. Margine, C. Verdi, and F. Giustino, Comput. Phys. Commun. **209**, 116 (2016).
[5] J. P. Perdew, K. Burke, and M. Ernzerhof, Phys. Rev. Lett. **77**, 3865 (1996).
[6] G. Pizzi, D. Volja, B. Kozinsky, M. Fornari, and N. Marzari, Comput. Phys. Commun. **185**, 422 (2014).
[7] X. Zeng, S. Zhao, Z. Li, and J. Yang, Phys. Rev. B **98**, 155443 (2018).
[8] T. Tada, S. Takemoto, S. Matsuishi, and H. Hosono, Inorg. Chem. **53**, 10347 (2014).
[9] W. Ming, M. Yoon, M.-H. Du, K. Lee, and S. W. Kim, J. Am. Chem. Soc. **138**, 15336 (2016).